Ultimate Stable Underwater Superhydrophobic State

Yaolei Xiang,[1] Shenglin Huang,[1] Pengyu Lv,[1] Yahui Xue,[1] Qiang Su,[1] and Huiling Duan[1,2,*]
[1]*State Key Laboratory for Turbulence and Complex Systems, Department of Mechanics and Engineering Science,*
BIC-ESAT, College of Engineering, Peking University, Beijing 100871, People's Republic of China
[2]*CAPT, HEDPS and IFSA Collaborative Innovation Center of MoE, Peking University,*
Beijing 100871, People's Republic of China

(Received 27 October 2016; revised manuscript received 8 March 2017; published 27 September 2017)

Underwater metastability hinders the durable application of superhydrophobic surfaces. In this work, through thermodynamic analysis, we theoretically demonstrate the existence of an ultimate stable state on underwater superhydrophobic surfaces. Such a state is achieved by the synergy of mechanical balance and chemical diffusion equilibrium across the entrapped liquid-air interfaces. By using confocal microscopy, we *in situ* examine the ultimate stable states on structured hydrophobic surfaces patterned with cylindrical micropores in different pressure and flow conditions. The equilibrium morphology of the meniscus is tuned by the dissolved gas saturation degree within a critical range at a given liquid pressure. Moreover, with fresh lotus leaves, we prove that the ultimate stable state can also be realized on randomly rough superhydrophobic surfaces. The finding here paves the way for applying superhydrophobic surfaces in environments with different liquid pressure and flow conditions.

DOI: 10.1103/PhysRevLett.119.134501

Biomimetic superhydrophobic surfaces have been demonstrated to be able to achieve significant drag reduction effects in both laminar and turbulent flows [1–5]. It relies on sustaining a large area fraction of shear-free liquid-air interfaces on these surfaces, that is, the so-called Cassie-Baxter (CB) state [6–12]. However, various factors, such as enhanced liquid pressure [13–19] and progressive reduction of air pressure in entrapped cavities due to air diffusion [20–23], have been observed to be able to induce the superhydrophobic wetting transition abruptly [16,17] or gradually with different time scales [20,24–26]. It contributes to prolonging the lifetime of the CB state by integrating sub-length-scale structures to resist high liquid pressure [27–30]. However, wetting transition induced by air diffusion is generally more critical, especially under high liquid pressure and flow conditions, resulting from the elevated gas diffusion flux [31–33]. A most recent experiment showed an underwater CB state with extended lifetime on grooved structures, which, on the other hand, is limited in quiescent water and hydrostatic pressure close to the atmospheric one [34]. It still lacks a good understanding of the underlying physics to realize sustainable underwater superhydrophobicity on arbitrary surface structures under different liquid pressure and flow conditions.

Here we explore the mechanism to achieve ultimate stability on underwater superhydrophobic surfaces with arbitrary structures and in different liquid pressures. The metastability of underwater superhydrophobicity has been widely observed previously [24,35], which, in fact, is attributed to the air diffusion induced unestablished equilibrium between the chemical potentials of the entrapped free gas in the cavities and the dissolved gas in the bulk water, leading to the collapse of the entrapped air. To access a long-term stable superhydrophobic state, we employ a thermodynamic free energy analysis of the submerged system, with the chemical potentials of the free gas in the cavities and the dissolved gas in the water being particularly taken into account. The latter has been generally omitted or ignored in previous thermodynamic analysis [35–38]. The present analysis leads to a both mechanically and chemically equilibrated superhydrophobic state, which hints unlimited sustainability of the underwater surface and thus is defined as an ultimate stable state. To verify the theoretical analysis, confocal microscopic experiments are carried out to demonstrate the ultimate stable state on both regularly and randomly structured hydrophobic surfaces in different liquid pressure and moderate flow rate conditions.

When a superhydrophobic surface with arbitrary topology is submerged underwater [see Fig. 1(a)], the equilibrium of the entrapped air cavities depends on the feasibility of the total free energy minimization of the thermodynamic system, consisting of bulk liquid in the reservoir (L), entrapped air [consisting of vapor (V) and free gas (G)], dissolved gas in the liquid, and all the interfaces between liquid, air, and solid. Based on thermodynamic analysis, the total free energy of the system is obtained as [39],

$$F_{\text{tot}} = (p_L - p_V - p_G)V_G + \gamma_{LG}(A_{LG} + A_{SG}\cos\theta_Y) + n_G RT \ln\frac{p_G}{s(p_L - p_V^*)} + n_V RT \ln\frac{p_V}{p_V^*} + F_0(p_L, T, s). \tag{1}$$

Here, p_G, p_V, and p_L are the entrapped gas, vapor, and liquid pressure [see Fig. 1(a)], V_G and n_G are the volume and mole number of entrapped gas, A_{LG} and A_{SG}

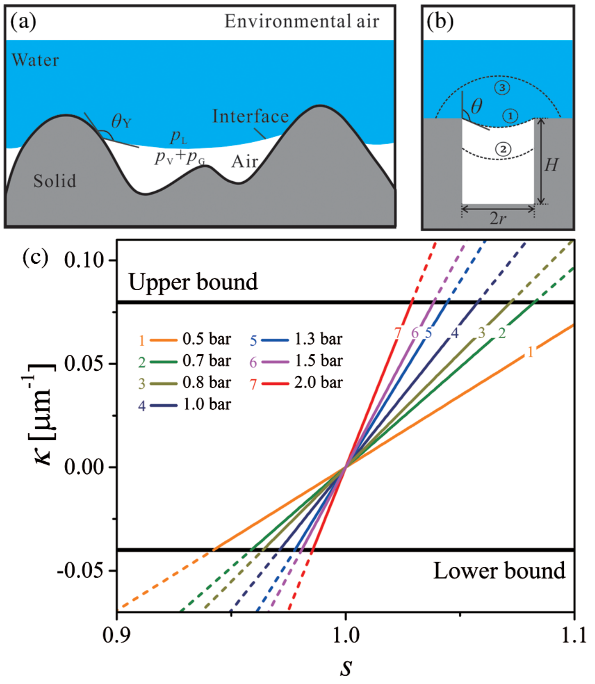

FIG. 1. Schematics of meniscus morphologies on submerged superhydrophobic surfaces with (a) arbitrary and (b) pore-patterned structures. Dashed lines in (b) show the pinned CB (1), depinned recession (2), and expansion (3) states, respectively. (c) Prediction of the equilibrium curvature (κ) dependence on the dissolved gas saturation degree (s) for different liquid pressures (p_L) on the pore-structured surface. Solid lines: stable states. Dashed lines: unstable states. Here, θ_a and θ_r are chosen as 120° and 95°, respectively, consistent with our experiments below.

are liquid-gas and solid-gas interface areas, and γ_{LG} and θ_Y are liquid-gas interface tension (0.0723 N/m for water at temperature, $T = 23\,°\mathrm{C}$) and contact angle, respectively. The dissolved gas saturation degree (s) in the bulk water at a given liquid pressure is defined by the ratio of the current dissolved gas concentration to the saturated one (e.g., $s = 1$ represents the saturated state). Consider a system with the volume of liquid reservoir much larger than the gas cavities consistent with our experiments below. It is reasonable to assume s is constant at a given liquid pressure and independent of the diffusion between air cavities and bulk water. Moreover, R is ideal gas constant, n_V is mole number of vapor in the cavity, and p_V^* represents the saturated vapor pressure, which is constant under thermostatic assumption. The first two terms on the right-hand side of Eq. (1) are attributed to the bulk and the interfaces, respectively. The third term, namely, the difference of chemical potential between free gas in the entrapped air and dissolved gas in the liquid causes alteration to the total free energy of the system. The fourth term describes the free energy contribution by unsaturated vapor in the closed air cavities [43]. The last term (F_0) on the right side of Eq. (1) is the free energy of a reference state, taken as the fully wetted Wenzel state. Here, F_0 is a constant for given liquid pressure (p_L), temperature (T), and dissolved gas saturation degree (s).

Then the final equilibrium state is derived by setting the first-order variation of the total free energy to zero, i.e., $\delta F_{\mathrm{tot}} = 0$ [39]. The first derivative with respect to the mole number of vapor in the cavity (n_V) leads to none other but the equilibrium between water and vapor, i.e., $p_V = p_V^*$. Here, both vapor and gas are assumed as ideal gases. By taking the volume of the entrapped air cavity and the mole number of the entrapped free gas as variables, we obtain two equations governing the equilibrium of the system, i.e.,

$$p_G + p_V - p_L = \gamma_{LG}\kappa, \tag{2}$$

$$p_G = s(p_L - p_V^*), \tag{3}$$

where κ is the meniscus curvature. Equation (2) is the Laplace equation, representing the mechanical balance of the meniscus, and Eq. (3) describes the chemical diffusion equilibrium between the dissolved gas in the liquid and the free gas entrapped in the cavities. Substituting Eq. (3) and vapor saturation condition ($p_V = p_V^*$) into Eq. (2) yields a general relation illustrating a both mechanically and chemically equilibrated state,

$$\gamma_{LG}\kappa = (p_L - p_V^*)(s - 1). \tag{4}$$

Equation (4) predicts the equilibrium morphology (κ) of the meniscus for given liquid pressure (p_L) and dissolved gas saturation degree (s). Thermodynamic stability analysis shows that the equilibrium state described by Eq. (4) can be both mechanically and chemically stable depending on surface morphology, namely, an ultimate stable state [39]. It will be demonstrated by our confocal experiments (as will be shown below).

We remark that the meniscus may detach from surface structures, e.g., according to the Gibbs' criterion for (de)pinning [44]. Feasible meniscus curvature (κ) is usually confined within a certain range on a specific surface structure, i.e., $[\kappa_{\min}, \kappa_{\max}]$, where $\kappa_{\min}$ and $\kappa_{\max}$ denote the minimum and maximum curvature values, respectively. Thus, according to Eq. (4), for a given liquid pressure (p_L), there exists a critical range of the dissolved gas saturation degree (s), within which the ultimate state can be achieved, that is,

$$1 + \gamma_{LG}\kappa_{\min}/(p_L - p_V^*) < s < 1 + \gamma_{LG}\kappa_{\max}/(p_L - p_V^*). \tag{5}$$

In this critical range, the ultimate stable morphology of the meniscus is controllable by adjusting s.

As an example we consider a structured surface patterned with cylindrical pores of radius ($r = 25\ \mu$m) and height ($H = 40\ \mu$m) submerged underwater [Fig. 1(b)]. The meniscus may pin at the pore corners, depin and sag into the pores, or expand on the structure surface, namely, the pinned Cassie-Baxter (CB), depinned recession, and expansion states, respectively [24,36]. Stability analysis of these different states indicates that the both mechanically and chemically equilibrated stable state can only be achieved in the pinned CB state [39], which thus will be our focus below. In the CB state, the meniscus curvature is given by $\kappa = 2\cos\theta/r$, where θ is the contact angle of the meniscus with the pore sidewall. According to the Gibbs' criterion for (de)pinning, θ is confined within $[\theta_r - \pi/2, \theta_a]$, where θ_r is the receding contact angle on the structure surface, and θ_a is the advancing contact angle of the pore sidewall. This leads to the upper and lower bounds of the meniscus curvature, where ultimate stability can be achieved, that is, $\kappa_{\min} = 2\cos\theta_a/r$ and $\kappa_{\max} = 2\sin\theta_r/r$ [see Fig. 1(c) and Fig. s3 in the Supplemental Material [39]]. Then the critical range of the dissolved gas saturation degree (s) at different liquid pressure is calculated by Eq. (5) and plotted in Fig. 1(c). Beyond this stable range, the meniscus will depin from the pore corners and then sag into the cavity until touching the bottom, or expand on the top surface until coalescence with nearby bubbles.

The above thermodynamic analysis clearly indicates an ultimate stable underwater superhydrophobic state that depends on the liquid pressure and dissolved gas saturation degree. In what follows, confocal microscopic experiments are carried out to probe the ultimate stable state.

A laser scanning confocal microscope (LSM 710, Carl Zeiss, Germany) with a 20× water immersion objective was employed to directly monitor the evolution of the samples under well-controlled conditions of liquid pressure, dissolved gas saturation degree, and fluid flow [see Fig. 2(a) and more details in the Supplemental Material [39]]. The samples with regularly patterned micropores of height ($H = 40$ μm) and radius ($r = 25$ μm) etched in silicon chips after hydrophobilization were used for convenient quantitative measurements [Fig. 2(b)]. Contact angles θ_a and θ_r on such pore-patterned samples were measured to be approximately 120° and 95°, respectively [24,36]. Fresh lotus leaves [Fig. 2(c)] were also utilized as samples to demonstrate the validation of the theory on randomly structured superhydrophobic surfaces, which will be shown in the later section.

The sample was fixed at the bottom of a rectangular flow channel with a top observing window for confocal microscopy and connected with a water tank for pressure control and water circulation. The liquid pressure in the tank was controlled mainly by the concentrated or reduced air pressure (p_a) and additionally by the water height (H_w) with respect to the sample surface, i.e., $p_L = \rho g H_w + p_a$, where ρ is water density, and g is the gravitational acceleration. Here, water volume in the tank was kept constant (approximately 0.7 L), and H_w was tuned by a lift platform. A dissolved oxygen meter was employed to monitor the dissolved gas concentration in deionized water. Prior to each experiment, the water had been equilibrated at the applied air pressure, p_a [as demonstrated in Fig. s6 of the Supplemental Material [39]]. After the dissolved oxygen meter showed a constant value for at least 20 min at a preset liquid pressure, the two valves for liquid flow were opened for water circulation with controlled flow rate up to 30 mL/min by a peristaltic pump [Fig. 2(a)]. Simultaneously, the confocal microscope was used to monitor the variation of the meniscus morphology with time by using a quick line-scanning mode, which takes approximately 10 s for each scan [24]. The meniscus curvature was then measured from the 2D meniscus profile [see Fig. s8 in the Supplemental Material [39]].

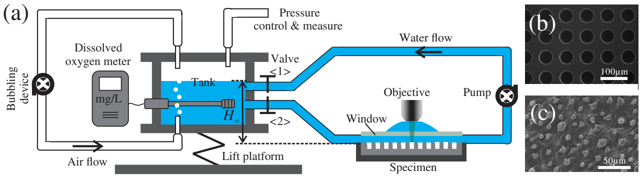

FIG. 2. (a) Schematics of the experiment setup. Confocal microscope is employed to examine the meniscus morphology on the specimen under different liquid pressure and flow rate. The gas dissolution in the water is assisted by a bubbling device. Scanning electronic microscopic (SEM) images show the surface structures of pore-patterned samples (b) and lotus leaf samples (c), respectively.

We remark that it is hard to achieve a long-term stable and direct-controlled dissolved gas saturation degree (s) in experiment [see Fig s7 in the Supplemental Material [39]]. Here we develop an alternative method to approach the problem. The long-term stable dissolved gas saturation degree (s) at liquid pressure (p_L) can be controlled by adjusting the water height (H_w) and/or the applied air pressure (p_a) in the present experiments. This is because the water is in fact saturated with dissolved gas at applied air pressure (p_a). Otherwise, gas dissolution will continuously evolve until saturation is reached. On the other hand, s is calculated with respect to the total liquid pressure (p_L). Thus, the relative contributions of $\rho g H_w$ and p_a to p_L determine s, that is, [39]

$$s = 1 - \rho g H_w/(\rho g H_w + p_a - p_V^*). \tag{6}$$

Accordingly, in our experiments we use H_w and p_a as adjusting parameters to achieve desired, long-term stable s and p_L. Specifically, substituting Eq. (6) into Eq. (4) yields a linear correlation between κ and H_w, i.e.,

$$\gamma_{LG}\kappa = -\rho g H_w. \tag{7}$$

Equation (7) implies that the control of the meniscus curvature by the water height is independent of the liquid pressure using the present experiment setup.

Figure 3(a) shows the curvature evolution of the meniscus under different air pressures (p_a) ranging from 0.5 to 2.0 bar with or without flow rate (e.g., $Q = 0$ or 23 mL/min) for two different water heights, $H_w = -13$ and 19 cm. The measured curvature indeed only shows dependence on the water height according to Eq. (7) and keeps almost constant during the 4 h observation for all experiment conditions [as shown in Fig. 3(a)]. We remark that the upper bound of the measured life span is only limited by the experiment setup itself. Thus the observation here clearly indicates an ultimate stable underwater superhydrophobic state in different liquid pressure and moderate flow rate conditions.

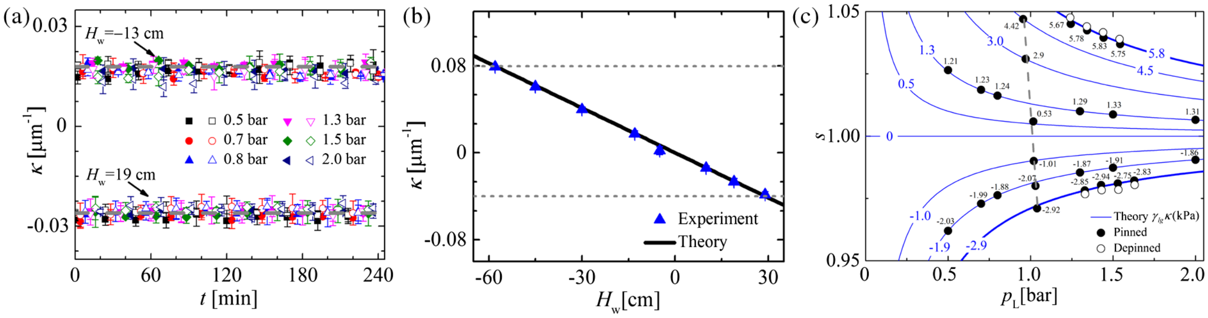

FIG. 3. (a) Variation of curvature (κ) as a function of time (t) under air pressure ranging from 0.5 to 2 bar with or without flow rate ($Q = 23$ mL/min) at two different water height, $H_w = 19$ and -13 cm. Solid dots: experiments in flow. Open dots: experiments in quiescent water. (b) Dependence of curvature (κ) on water height (H_w) at a constant air pressure, $p_a = 1.2$ bar. Dots: experiments. Solid line: theoretical prediction. Dashed lines: predicted upper and lower curvature bounds, respectively. (c) Contour plot of $\gamma_{LG}\kappa$ as a function of liquid pressure (p_L) and dissolved gas saturation degree (s) in the pinned CB state according to Eq. (4). Numbers with unit [kPa] indicate the values of $\gamma_{LG}\kappa$ for the corresponding lines or dots. Solid lines: theoretical prediction. Solid and open dots: experiments in pinning stable and depinned unstable states, respectively. The dashed line shows a series of experiments carried out by maintaining the air pressure in the tank.

Moreover, the equilibrium curvature (κ) as a function of the water height (H_w) was measured at a constant air pressure in the tank, e.g., $p_a = 1.2$ bar. The plot in Fig. 3(b) verifies the linear correlation between κ and H_w as predicted by Eq. (7), indicating the meniscus morphology can be independently controlled by the water height in the present experiments.

To see more clearly how the ultimate stable state depends on the liquid pressure and dissolved gas saturation degree as predicted by Eq. (4) in a more general case, we examine the contour plots of $\gamma_{LG}\kappa$ as a function of p_L and s in Fig. 3(c). The experiment data along each contour were obtained by maintaining a constant liquid height (H_w) while tuning the air pressure (p_a) in the tank. On the other hand, H_w could also be regulated to achieve different values of $\gamma_{LG}\kappa$ while keeping the air pressure as a constant. The obtained experiment data are shown along the dashed line in Fig. 3(c). Here, s is directly calculated according to the measurements of the dissolved oxygen meter, which shows consistent results with the calculation by Eq. (6) [39]. The predicted upper and lower bounds of $\gamma_{LG}\kappa$ for achievable pinned states are 5.8 and -2.9 kPa, respectively [as shown by the thick blue lines in Fig. 3(c)]. Within the two bounds [as described by Eq. (5)], the ultimate stable state can be achieved, as proved by the experiment data of those solids dots in Fig. 3(c). The measured curvature values show a good agreement with the theoretical predictions by Eq. (4). The overall curvature error is within 7%, indicating the accuracy of the meniscus morphology control in the present experiments. It is also seen that the stable range of s decreases with the liquid pressure, agreeing well with the tendency prediction by Fig. 1(c).

On the other hand, beyond these two bounds, the meniscus becomes metastable or even unstable, leading to its depinning from pore corners and subsequent sagging into the air cavity or expanding on the upper structure surface [see Fig. s9 in the Supplemental Material [39]]. Those experiment data are marked as open circles in Fig. 3(c). The instability and recession of these depinned states have also been widely investigated in Refs. [21,24,25,34,36] and thus are not our present focus.

In order to prove the validation of the present framework on randomly structured superhydrophobic surfaces, we investigate the ultimate stability of self-cleaning lotus leaves submerged underwater, e.g., at a pressure of 1.5 bar and a flow rate of 23 mL/min. Figures 4(a) and 4(b) show the snapshots of the evolution of the air cushion on the lotus leave immersed in water saturated with air (i.e., $s = 1$). It is surprising to find that the air cushion keeps almost flat and shows no tendency to decay over 4 h [see attached video in the Supplemental Material [39]]. In contrast, the lotus leave submerged under air-unsaturated water with $s = 0.67$, which is beyond the critical sable range of s, only sustains its superhydrophobicity within 2 min, as shown in Figs. 4(c) and 4(d). This is the same with the usual observation of underwater metastability of lotus leaves [13,14]. Detailed three-dimensional images of the sustained and collapsed interfaces of lotus leaves can be found in Fig. s10 in the Supplemental Material [39]. Thus, the ultimate stable state predicted by Eq. (4) can not only be achieved on regularly patterned structures but also on random surface structures.

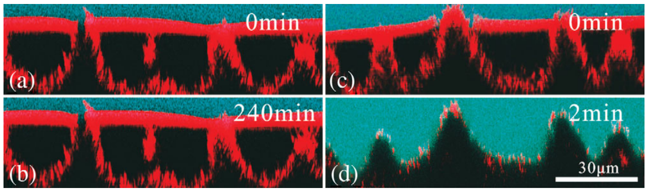

FIG. 4. Snapshots of confocal microscopy images showing the long-term stable (a), (b) and unstable (c), (d) lotus leave surfaces under a liquid pressure of 1.5 bar and a flow rate of 23 mL/min. In (a) and (b), the dissolved gas saturation degree, $s = 1$. And in (c) and (d), $s = 0.67$. The blue region indicates water. The planar red surface is the water-air interface. The red rough part beneath is the microstructure of the lotus leave.

The key is to maintain both mechanical balance and chemical diffusion equilibrium at the submerged superhydrophobic surfaces.

In summary, through thermodynamics analysis with considering the chemical potential of dissolved gas in water, we predict an ultimate stable superhydrophobic state submerged underwater, which is both mechanically and chemically equilibrated. We have carried out confocal microscopic experiments and directly observed the ultimate stable underwater superhydrophobic state. It is evident that the equilibrium morphology of the meniscus is controllable by adjusting the dissolved gas saturation degree within a critical range for given liquid pressure. Last but not least, in contrast to the preceding metastable observation, we have also demonstrated the ultimate stable superhydrophobicity on submerged fresh lotus leaves with random surface structures. The current work implies that the ultimate stable state can be achieved in different pressure, arbitrary rough superhydrophobic surface and even flow conditions. Moreover, the present theory is not stipulated on hydrophobic structures. It may even open the avenue to realize ultimate stable superhydrophobic states on hydrophilic structured surfaces. The finding here contributes to a better understanding of the underlying mechanism of long-term stability of underwater superhydrophobicity and also promotes the wide application of these surfaces in various environments.

The following agencies and programs are acknowledged: This work was supported by National Natural Science foundation of China (NSFC) under Grants No. 11521202 and No. 11632001. The authors thank the Core Facilities at School of Life Sciences, Peking University for assistance with Confocal Microscopy.

---

[*] Corresponding author.
hlduan@pku.edu.cn

[1] J. P. Rothstein, Annu. Rev. Fluid Mech. **42**, 89 (2010).
[2] B. Bhushan and Y. C. Jung, Prog. Mater. Sci. **56**, 1 (2011).
[3] Y. H. Xue, P. Y. Lv, H. Lin, and H. L. Duan, Appl. Mech. Rev. **68**, 030803 (2016).
[4] G. McHale, M. I. Newton, and N. J. Shirtcliffe, Soft Matter **6**, 714 (2010).
[5] O. I. Vinogradova and A. V. Belyaev, J. Phys. Condens. Matter **23**, 184104 (2011).
[6] A. B. D. Cassie and S. Baxter, Trans. Faraday Soc. **40**, 546 (1944).
[7] L. Feng, S. H. Li, Y. S. Li, H. J. Li, L. J. Zhang, J. Zhai, Y. L. Song, B. Q. Liu, L. Jiang, and D. B. Zhu, Adv. Mater. **14**, 1857 (2002).
[8] D. Quéré, Annu. Rev. Mater. Res. **38**, 71 (2008).
[9] R. A. Verschoof, R. C. A. van der Veen, C. Sun, and D. Lohse, Phys. Rev. Lett. **117**, 104502 (2016).
[10] T. Y. Liu and C. J. Kim, Science **346**, 1096 (2014).
[11] S. Lee, J. Lee, J. Park, Y. Choi, and K. Yong, Adv. Mater. **24**, 2418 (2012).
[12] O. I. Vinogradova and A. L. Dubov, Mendeleev Commun. **22**, 229 (2012).
[13] S. Herminghaus, Europhys. Lett. **52**, 165 (2000).
[14] J. H. Zhang, X. L. Sheng, and L. Jiang, Langmuir **25**, 1371 (2009).
[15] A. Lafuma and D. Quéré, Nat. Mater. **2**, 457 (2003).
[16] P. Forsberg, F. Nikolajeff, and M. Karlsson, Soft Matter **7**, 104 (2011).
[17] L. Lei, H. Li, J. Shi, and Y. Chen, Langmuir **26**, 3666 (2010).
[18] A. Checco, B. M. Ocko, A. Rahman, C. T. Black, M. Tasinkevych, A. Giacomello, and S. Dietrich, Phys. Rev. Lett. **112**, 216101 (2014).
[19] Q. S. Zheng, Y. Yu, and Z. H. Zhao, Langmuir **21**, 12207 (2005).
[20] R. Poetes, K. Holtzmann, K. Franze, and U. Steiner, Phys. Rev. Lett. **105**, 166104 (2010).
[21] M. S. Bobji, S. V. Kumar, A. Asthana, and R. N. Govardhan, Langmuir **25**, 12120 (2009).
[22] M. A. Samaha, H. V. Tafreshi, and M. G. el Hak, Langmuir **28**, 9759 (2012).
[23] R. N. Govardhan, G. S. Srinivas, A. Asthana, and M. S. Bobji, Phys. Fluids **21**, 052001 (2009).
[24] P. Lv, Y. Xue, Y. Shi, H. Lin, and H. Duan, Phys. Rev. Lett. **112**, 196101 (2014).
[25] D. Dilip, N. K. Jha, R. N. Govardhan, and M. S. Bobji, Colloids Surf. A **459**, 217 (2014).
[26] J. H. Weijs and D. Lohse, Phys. Rev. Lett. **110**, 054501 (2013).
[27] Y. H. Xue, S. G. Chu, P. Y. Lv, and H. L. Duan, Langmuir **28**, 9440 (2012).
[28] A. Balmert, H. F. Bohn, P. Ditsche-Kuru, and W. Barthlott, J. Morphol. **272**, 442 (2011).
[29] M. Lee, C. Yim, and S. Jeon, Appl. Phys. Lett. **106**, 011605 (2015).
[30] Y. W. Su, B. H. Ji, K. Zhang, H. J. Gao, Y. G. Huang, and K. Hwang, Langmuir **26**, 4984 (2010).
[31] Y. L. Xiang, Y. H. Xue, P. Y. Lv, D. D. Li, and H. L. Duan, Soft Matter **12**, 4241 (2016).
[32] C. Barth, M. Samaha, H. Tafreshi, and M. Gad-el-Hak, Int. J. Flow Control **5**, 79 (2013).
[33] E. Karatay, P. A. Tsai, and R. G. H. Lammertink, Soft Matter **9**, 11098 (2013).
[34] M. Xu, G. Sun, and C. J. Kim, Phys. Rev. Lett. **113**, 136103 (2014).
[35] A. Giacomello, M. Chinappi, S. Meloni, and C. M. Casciola, Phys. Rev. Lett. **109**, 226102 (2012).
[36] Y. H. Xue, P. Y. Lv, Y. Liu, Y. P. Shi, H. Lin, and H. L. Duan, Phys. Fluids **27**, 092003 (2015).
[37] A. Marmur, Langmuir **22**, 1400 (2006).
[38] N. A. Patankar, J. Adhes. Sci. Technol. **23**, 413 (2009).
[39] See Supplemental Material at http://link.aps.org/supplemental/10.1103/PhysRevLett.119.134501 for further details on theoretical derivations, experimental system, dissolved gas saturation degree, and meniscus morphology measurements, which includes Refs. [40–42].
[40] L. D. Landau and E. M. Lifshitz, *Statistical Physics*, Vol. 5 (Pergamon Press, Oxford, 1980), Part 1.
[41] T. Frankel, *The Geometry of Physics: An Introduction* (Cambridge University Press, Cambridge, England, 2011).
[42] N. Patankar, Langmuir **32**, 7023 (2016).
[43] M. Yarom and A. Marmur, Langmuir **31**, 7792 (2015).
[44] J. W. Gibbs, *The Scientific Papers of J. Willard Gibbs* (Longmans-Green, London, 1906), Vol. 1.